Supplemental Material
Electron Mobilities in $SrTiO_3$ and $KTaO_3$: Role of Phonon Anharmonicity, Mass Renormalization and Disorder

Luigi Ranalli,[1,2,*] Carla Verdi,[3] Marios Zacharias,[4] Jacky Even,[4] Feliciano Giustino,[5,6] and Cesare Franchini[1,7]

[1] *Faculty of Physics and Center for Computational Materials Science, University of Vienna, Kolingasse 14-16, 1090 Vienna, Austria*
[2] *Vienna Doctoral School in Physics, University of Vienna, Boltzmanngasse 5, 1090 Vienna, Austria*
[3] *School of Mathematics and Phisycs, University of Queensland, 4072 Brisbane, Queensland, Australia*
[4] *Univ Rennes, INSA Rennes, CNRS, Institut FOTON - UMR 6082, F-35000 Rennes, France*
[5] *Oden Institute for Computational Engineering and Sciences, The University of Texas at Austin, Austin, Texas 78712, USA*
[6] *Department of Physics, The University of Texas at Austin, Austin, Texas 78712, USA*
[7] *Department of Physics and Astronomy "Augusto Righi" Alma Mater Studiorum - Università di Bologna, 40127 Bologna Italy*

(Dated: September 13, 2024)

I. PHONON-LIMITED DRIFT MOBILITY

The equilibrium electric current $\mathbf{J}$ in a semiconductor is related to the external electric field $\mathbf{E}$ via:

$$J_\alpha = e(n_e\mu_{e,\alpha\beta} + n_h\mu_{h,\alpha\beta})E_\beta, \tag{S1}$$

where $\mu_{e,\alpha\beta}$ and $\mu_{h,\alpha\beta}$ are the electron and hole mobility tensors, respectively, and the Greek indices denote Cartesian coordinates. The current density can also be expressed as an integral over the first Brillouin zone [1]:

$$J_\alpha = -e\Omega\sum_n \Omega_{BZ}^{-1}\int d\mathbf{k} f_{n\mathbf{k}} v_{n\mathbf{k},\alpha}, \tag{S2}$$

where Ω and Ω_{BZ} are the unit-cell and BZ volumes respectively, $v_{n\mathbf{k},\alpha} = \hbar^{-1}\partial\epsilon_{n\mathbf{k}}/\partial k_\alpha$ is the band velocity and $f_{n\mathbf{k}}$ is the electronic occupation function, which reduces to the Fermi-Dirac distribution $f^0_{n\mathbf{k}}$ in the absence of an electric field. By deriving the current with respect to the electric field, the electron mobility is expressed as:

$$\mu_{e,\alpha\beta} = -\frac{\sum_{n\in\mathrm{CB}}\int d\mathbf{k} v_{n\mathbf{k},\alpha}\partial_{E_\beta} f_{n\mathbf{k}}}{\sum_{n\in\mathrm{CB}}\int d\mathbf{k} f^0_{n\mathbf{k}}}, \tag{S3}$$

where CB indicates the conduction bands. The response $\partial_{E_\beta} f_{n\mathbf{k}}$ can be computed starting from the BTE [1]:

$$\begin{aligned}
&-e\mathbf{E}\cdot\frac{1}{\hbar}\partial_{\mathbf{k}} f_{n\mathbf{k}} = \frac{2\pi}{\hbar}\sum_{m\nu}\int\frac{d\mathbf{q}}{\Omega_{BZ}}|g_{mn\nu}(\mathbf{k},\mathbf{q})|^2\\
&\times[f_{n\mathbf{k}}(1-f_{m\mathbf{k+q}})\delta(\epsilon_{n\mathbf{k}}-\epsilon_{m\mathbf{k+q}}+\hbar\omega_{\mathbf{q}\nu})n_{\mathbf{q}\nu}\\
&+ f_{n\mathbf{k}}(1-f_{m\mathbf{k+q}})\delta(\epsilon_{n\mathbf{k}}-\epsilon_{m\mathbf{k+q}}-\hbar\omega_{\mathbf{q}\nu})(1+n_{\mathbf{q}\nu})\\
&- f_{m\mathbf{k+q}}(1-f_{n\mathbf{k}})\delta(\epsilon_{m\mathbf{k+q}}-\epsilon_{n\mathbf{k}}-\hbar\omega_{\mathbf{q}\nu})(1+n_{\mathbf{q}\nu})\\
&- f_{m\mathbf{k+q}}(1-f_{n\mathbf{k}})\delta(\epsilon_{m\mathbf{k+q}}-\epsilon_{n\mathbf{k}}+\hbar\omega_{\mathbf{q}\nu})n_{\mathbf{q}\nu}],
\end{aligned} \tag{S4}$$

where $g_{mn\nu}(\mathbf{k},\mathbf{q})$ is the electron-phonon matrix element [2,3] of Eq. (1) in the main text. By taking the derivative of Eq. (S4) with respect to $\mathbf{E}$ the linearized BTE is obtained:

$$\begin{aligned}
&\partial_{E_\beta} f_{n\mathbf{k}} = e\partial_{\epsilon_{n\mathbf{k}}} f^0_{n\mathbf{k}} v_{n\mathbf{k},\beta}\tau^0_{n\mathbf{k}}\\
&+\frac{2\pi\tau^0_{n\mathbf{k}}}{\hbar}\sum_{m\nu}\int\frac{d\mathbf{q}}{\Omega_{BZ}}|g_{mn\nu}(\mathbf{k},\mathbf{q})|^2\\
&\times[(1+n_{\mathbf{q}\nu}-f^0_{n\mathbf{k}})\delta(\epsilon_{n\mathbf{k}}-\epsilon_{m\mathbf{k+q}}+\hbar\omega_{\mathbf{q}\nu})\\
&+(n_{\mathbf{q}\nu}+f^0_{n\mathbf{k}})\delta(\epsilon_{n\mathbf{k}}-\epsilon_{m\mathbf{k+q}}-\hbar\omega_{\mathbf{q}\nu})]\partial_{E_\beta} f_{m\mathbf{k+q}},
\end{aligned} \tag{S5}$$

where the relaxation time $\tau^0_{n\mathbf{k}}$ is defined as:

$$\begin{aligned}
\frac{1}{\tau^0_{n\mathbf{k}}} &= \frac{2\pi}{\hbar}\sum_{m\nu}\int\frac{d\mathbf{q}}{\Omega_{BZ}}|g_{mn\nu}(\mathbf{k},\mathbf{q})|^2\\
&\times[(1-f^0_{m\mathbf{k+q}}+n_{\mathbf{q}\nu})\delta(\epsilon_{n\mathbf{k}}-\epsilon_{m\mathbf{k+q}}-\hbar\omega_{\mathbf{q}\nu})\\
&+(f^0_{m\mathbf{k+q}}+n_{\mathbf{q}\nu})\delta(\epsilon_{n\mathbf{k}}-\epsilon_{m\mathbf{k+q}}+\hbar\omega_{\mathbf{q}\nu})].
\end{aligned} \tag{S6}$$

Eq. (S5) is valid in the limit of low electric field-induced energy gain with respect to the thermal energy: $eE_\beta v_{n\mathbf{k},\beta}\tau^0_{n\mathbf{k}} << k_BT$. The iterative BTE scheme (IBTE) consists in solving Eq. (S5) self-consistently, while the simpler self-energy relaxation time approximation (SERTA) ignores the integral in $d\mathbf{q}$. In this case, the mobility reduces to:

$$\mu^{\mathrm{SERTA}}_{e,\alpha\beta} = \frac{-e}{n_e\Omega}\sum_{n\in\mathrm{CB}}\frac{d\mathbf{k}}{\Omega_{\mathrm{BZ}}}\partial_{\epsilon_{n\mathbf{k}}} f^0_{n\mathbf{k}} v_{n\mathbf{k},\beta}\tau^0_{n\mathbf{k}}. \tag{S7}$$

In our work, we adopt 100×100×100 k- and q-grids for the drift and Hall mobility calculations at the RTA and IBTE levels. In Fig. S1 we show a set of convergence tests for the IBTE drift and Hall mobility in $SrTiO_3$ and $KTaO_3$ at 300 K.

II. ANHARMONIC CORRECTIONS TO THE ELECTRON-PHONON MATRIX ELEMENTS

To incorporate phonon anharmonicity in our calculations, the electron-phonon matrix elements are computed by using the harmonic derivatives of the self-consistent potential, together with the temperature-dependent anharmonic eigenfrequencies and eigenvectors, as explained in the main text (Sec. IIA).

To demonstrate the validity of this procedure, as in Ref. [4], we have compared in Fig. S2(a) the $SrTiO_3$ electron-phonon matrix elements obtained from

* Email: luigi.ranalli@univie.ac.at

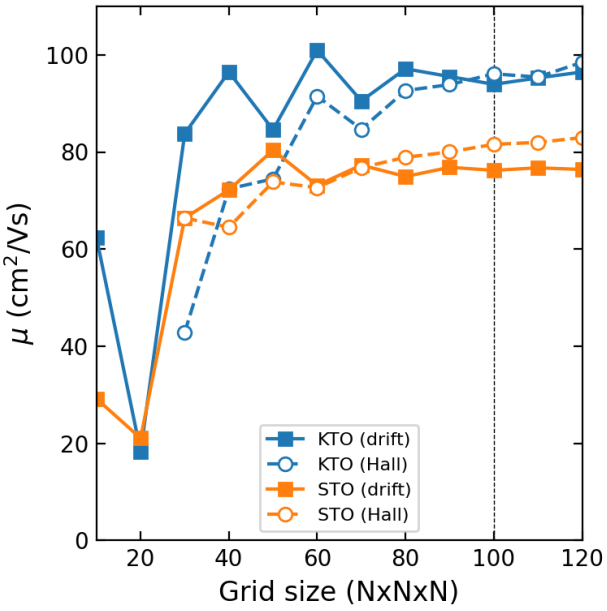

FIG. S1: Convergence of the drift and Hall mobilities in $KTaO_3$ and $SrTO_3$ without SOC at 300 K. The dashed vertical line highlights the 100×100×100 reciprocal grid employed for all mobility calculations.

fully harmonic density functional perturbation theory (DFPT) calculations with the ones obtained by substituting anharmonic phonons. We show the square root of the gauge-invariant trace of $|g_{mn\nu}(\mathbf{k},\mathbf{q})|^2$. In particular, we have considered the coupling of the 3 lowest conduction bands at the Γ-point (in k-space) with each phonon branch along a high-symmetry q-path. The artificial divergences caused by the imaginary frequencies of the ferrodistortive (FE) and antiferrodistortive (AFD) modes are correctly renormalized. On the other hand, the overall behavior away from those regions is unchanged, since the anharmonic renormalization affects mostly the soft FE and AFD modes. In Fig. S2(b) the anharmonic phonon dispersions obtained from the SSCHA free-energy Hessian are shown together with the squared traces of the matrix elements at the Γ-point (in k-space), highlighting the importance of the three longitudinal optical (LO) modes especially at long wavelengths. Similar results are shown in Fig. S2(c)-(d) for $KTaO_3$. In this case, the DFPT harmonic dynamical matrices are positive definite. The coupling strength in Fig. S2(d) is analogous to the one obtained for $SrTiO_3$.

III. WANNIERIZATION OF THE DISORDERED BANDS

The disordered 2×2×2 supercell constituting the ground state of $SrTiO_3$ is shown in Fig. S3. The spectral function resulting from unfolding the conduction bands onto the 1BZ of the cubic unit cell is shown in Fig. S4 and Fig. 3 in the main text, exhibiting some low-weight features at higher energies. Since the electron energy window that effectively contributes to conduction is approximately 0.2 eV from the conduction-band bottom, these features do not contribute to our mobility calculations.

Near the conduction band bottom, the quasiparticle picture is preserved. In order to construct the Wannier functions for the 3 lowest conduction bands, we start from the Kohn-Sham wavefunctions and energies calculated on a 4×4×4 k-point grid (consistent with the 8×8×8 employed for the unit cell) and select the well-defined eigenvalues with large spectral weight for each k-point. This way, we obtain 3 eigenvalues for each k-point, analogously to the unit-cell case. The accuracy of the Wannier interpolation of the unfolded bands shown in Fig. S4 validates our procedure.

IV. DETAILS ON THE MLFF

In polar materials in the $\mathbf{q} \to 0$ limit, a macroscopic electric field appears as a consequence of the long-range character of the Coulomb interaction. A simple Fourier interpolation of the force constants would thus fail for the dynamical matrix $\Phi(\mathbf{q})$ around $\mathbf{q} = 0$. The typical strategy [5] consists of interpolating only the short-range component of the force constants after the long-range one has been subtracted in the supercell considered. The long-range dipole-dipole contribution to the dynamical matrix is then added for every q-point in the Brillouin zone.

When using a machine learning force field (MLFF) for the calculation of the interatomic forces, the cut-off radius introduced for both the radial and angular local descriptors may result in some artificial "wigglings" of the phonon eigenfrequencies around the Γ point. This effect appears when the cut-off radius is smaller than the supercell size adopted during training. In this case, the dipole-dipole component of the interatomic force constants subtracted before interpolation may not correspond to the effective range of interatomic forces captured by the MLFF. In fact, we find that using a large cut-off radius of 13 Å for the descriptors eliminates this spurious effect, as shown in Fig. S5(a) for the highest frequency longitudinal optical (LO) mode. This cut-off is of the same order as the supercell size used to calculate the force constants.

This precaution comes with a slight worsening in the accuracy of the MLFF for the root mean square error (RMSE) of the energies on a test dataset. The test datasets are extracted from MD simulations between 0 K and 400 K. For $SrTiO_3$, 25 structures of 10-atom cells are extracted from a fixed-pressure (NPT) simulation in order to validate the accuracy of the MLFF with respect to RPA data. For $KTaO_3$, 25 structures from a fixed-volume (NVT) simulation of the larger 4×4×4 supercell were extracted, since the SCAN calculations are feasible in this larger supercell.

In the case of $SrTiO_3$ in Fig. S5(b), the RMSE slightly increases with the cut-off radii, while for $KTaO_3$ it remains stable when increasing the cut-off, as shown in Fig. S6(a). However, if the test structures are extracted from an NPT simulation (that is, we let the volume vary at fixed 0 GPa pressure) rather than NVT, the RMSE increases with the cut-off radii, as shown in Fig. S6(b). By expanding the training set with 677 configurations from an NPT simulation between 0 K and 400 K, the performance of the MLFF becomes consistent across the NVT and NPT datasets, as shown in Fig. S6(c)-

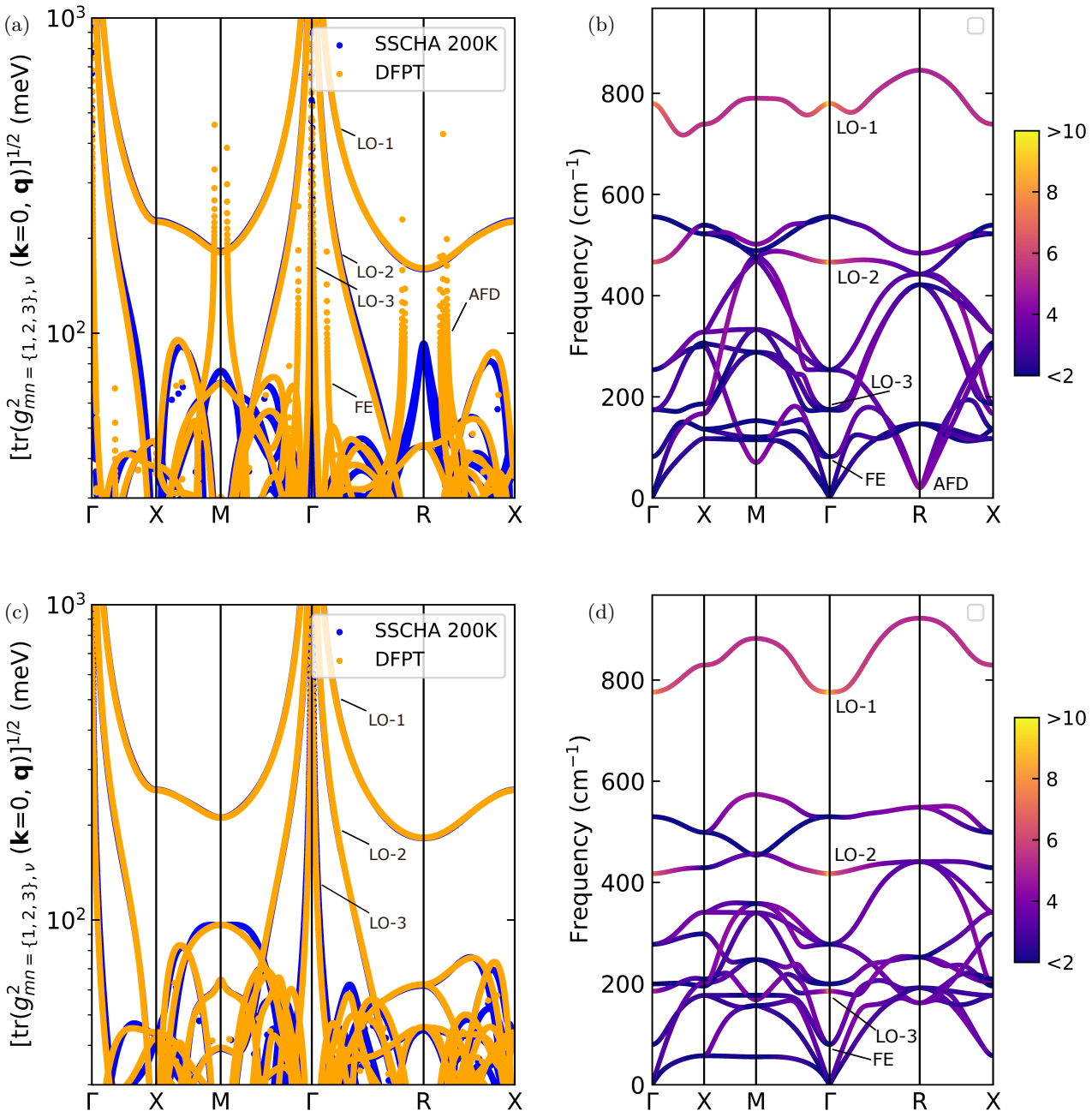

FIG. S2: Comparison of the electron-phonon matrix elements for (a) $SrTiO_3$ and (c) $KTaO_3$ obtained by employing the harmonic dynamical matrices and the SSCHA free-energy Hessian matrices at 200 K. The phonon dispersions plotted with a colour map of the electron-phonon matrix elements for each phonon branch $g_\nu(\mathbf{q})$ are shown for (b) $SrTiO_3$ and (d) $KTaO_3$.

(d). The expanded NPT training dataset was not employed for $KTaO_3$ in this study, but rather the NVT one, since it is faster and delivers the same accuracy in the configuration space of interest [Fig. S7(b)]. The NPT-expanded MLFF may be employed for different purposes and serves here as a proof of concept for the consistency of the cut-off increase choice.

Note that the larger error in the energies per atom in the case of $SrTiO_3$ as compared to $KTaO_3$, where the test calculations are performed using larger supercells, is due to simple error propagation with respect to the system size, with the energy per atom RMSE scaling as $1/\sqrt{N}$ (N is the system size). We also notice that the scaling of the NPT validation RMSE in Fig. S6(d) is better than the $SrTiO_3$ case in Fig. S5(b). This may be due to the fact that in $SrTiO_3$, we have used the Δ-ML method to learn an RPA-level MLFF on top of a baseline DFT one [6], and the resulting MLFF may more easily overfit the NPT configuration space when increasing the cut-off radii.

V. DETAILS ON THE MLFF+SSCHA CALCULATIONS

The stochastic self-consistent harmonic approximation (SSCHA) calculations performed in this work were automated with the aid of the Atomic Simulation Environ-

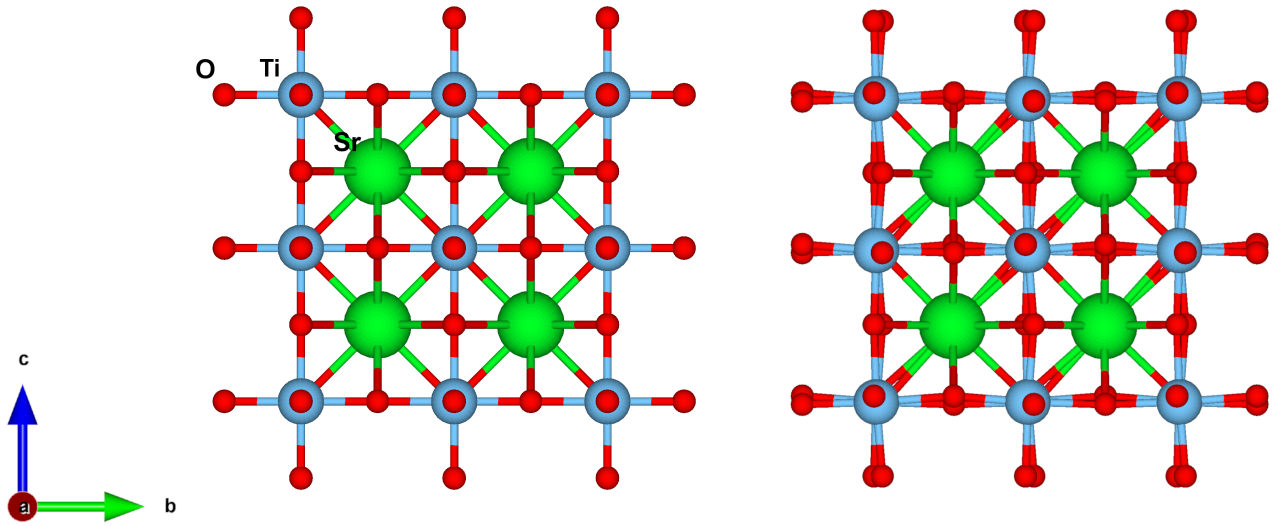

FIG. S3: Comparison between the $SrTiO_3$ symmetric cubic structure (left) and the disordered one (right).

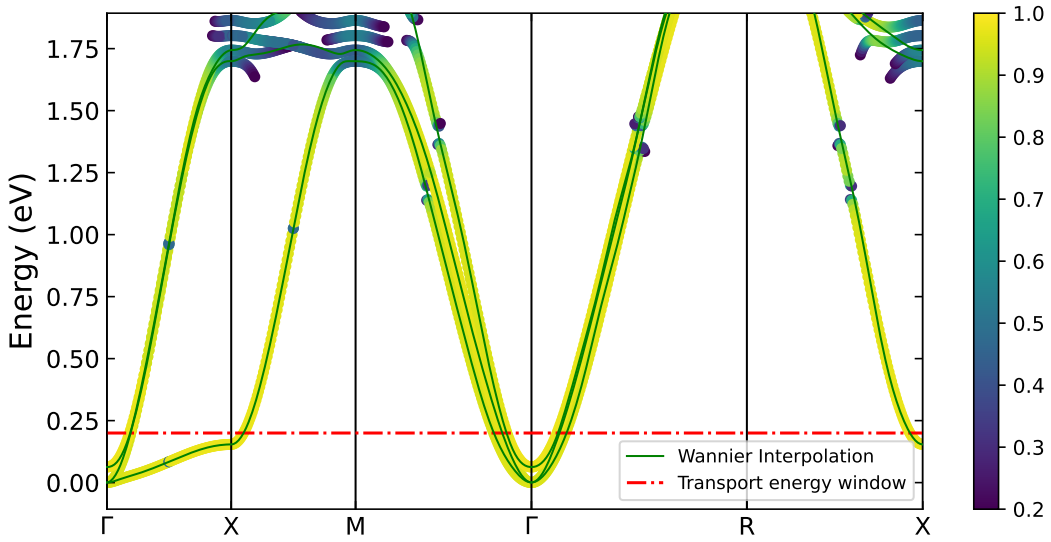

FIG. S4: Spectral function of disordered $SrTiO_3$ calculated using a $2 \times 2 \times 2$ supercell and unfolded. Only the peaks with spectral weight larger than 0.2 are shown. The Wannier interpolation on the high-symmetry path accurately reproduces the unfolded band structure around the energy window contributing to electronic transport, validating the eigenvalue extraction and Wannier interpolation procedure.

ment (ASE) package, with an in-house modification of both ASE and SSCHA.

The self-consistent loop was solved by generating 800 ensembles for each population, the Kong-Liu effective ratio was set to 0.8, the preconditioning of the dynamical matrix was kept active, and the "normal" root representation was chosen. Finally, the free-energy Hessian at each temperature, which includes the static "bubble" correction to the self-consistent SSCHA frequencies [7]), was computed using an ensemble of 5000 structures.

The frequencies obtained from the free-energy Hessian (SSCHA+Bubble) for the temperature-dependent anharmonic FE soft mode at Γ in $KTaO_3$ are in good agreement with experimental measures [8], as shown in Fig. S7(a). Interpolating the bubble correction using a 20×20×20 q-grid [7] yields fully converged frequencies that differ by less than 6 cm^{-1} from the non-interpolated values along the whole temperature range. For practical reasons, mobility calculations for $SrTiO_3$ and $KTaO_3$ have thus been performed using the bubble-corrected dynamical matrices (free-energy Hessians) without interpolation.

As stated in Section IV, the validation tests demonstrate how using an NVT-MD is suitable for building a MLFF to be employed for SSCHA at the same fixed volume V. This is demonstrated in Fig. S7(b), showing the $KTaO_3$ Γ-point FE frequency as a function of temperature. The NPT MLFF and the NVT MLFF yield very similar frequency predictions in the range of temperatures of interest for the mobility calculations.

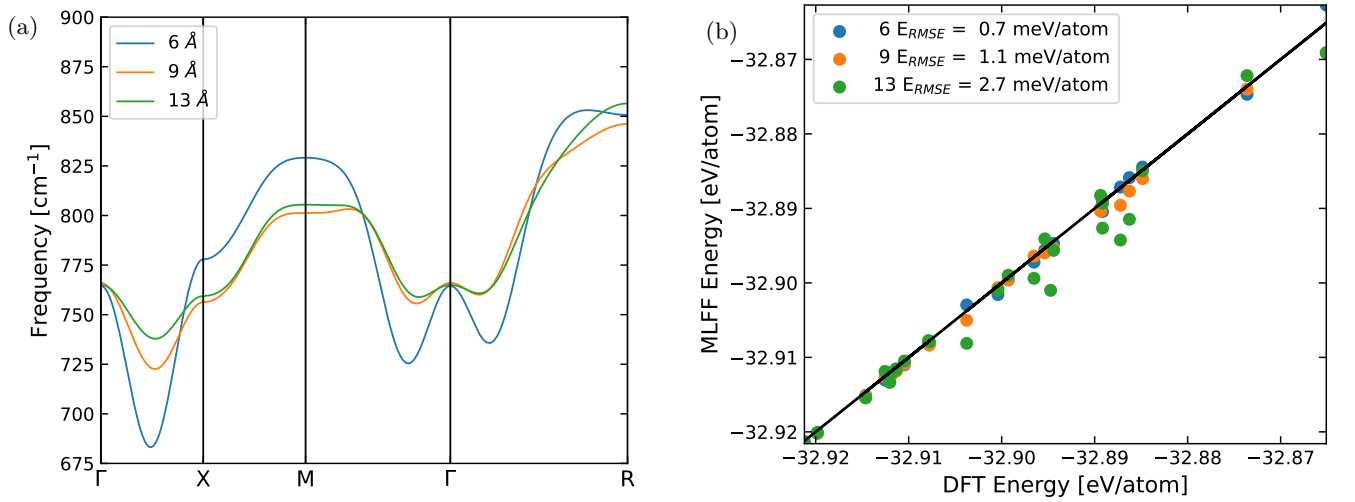

FIG. S5: Accuracy of the MLFF for SrTiO3. (a) Highest frequency LO branch as computed by MLFF at the harmonic level using force constants interpolated from a 4×4×4 supercell. The artificial wiggling around the Γ-point is cured by increasing the cut-off radius for the radial and angular descriptors. (b) Energy RMSE on the RPA test set using different values for the cut-off radii.

TABLE SI: Conduction-band effective masses with|without spin-orbit coupling for $SrTiO_3$ in the ordered (cubic) and disordered structure, and for $KTaO_3$ in the ground-state cubic structure. m^*_{he} stands for the heavy electron mass, $m^*_{le_1}$ and $m^*_{le_2}$ for the light electron masses.

	Path	m^*_{he}	$m^*_{le_1}$	$m^*_{le_2}$
$SrTiO_3$	Γ– R	0.62|0.67	0.53|0.53	0.57|0.53
	Γ– X	1.10|6.37	0.39|0.39	0.54|0.39
	Γ– M	0.74|0.88	0.47|0.64	0.54|0.39
$KTaO_3$	Γ– R	0.46|0.50	0.38|0.41	0.44|0.41
	Γ– X	0.78|5.30	0.28|0.30	0.45|0.30
	Γ– M	0.55|0.65	0.33|0.50	0.44|0.30

VI. ADDITIONAL MOBILITY RESULTS

The electron-phonon matrix elements associated with imaginary phonon modes are conventionally set to zero. This can lead to spurious mobility modifications when said imaginary modes would scatter considerably with carriers. In $SrTiO_3$ at the harmonic level of theory, the AFD mode is imaginary at the R-point close to the cubic-to-tetragonal phase transition, and it experiences a strong positive renormalization when increasing the temperature. The same happens for the Γ-point FE mode, associated to the ferroelectric instability.

As shown in Fig. S8, excluding these modes brings a strongly overestimated mobility at around 150 K, where their contribution to the electron scattering would be greater due to the softer frequency. The difference with a fully anharmonic treatment instead vanishes at room temperature, where these modes are harder and the associated electron-phonon scattering weaker. We remark that when calculating the electron mobilities using harmonic dynamical matrices in Fig. S8, a cut-off of 10 meV on the phonon frequencies was set in order to fully exclude scattering from those branches that become imaginary. Not setting this cut-off leads to an overestimated scattering due to the spurious divergence of the electron-phonon matrix elements and thus a lower mobility that has no physical meaning.

In Fig. S9 we compare the electron mobility computed for both $SrTiO_3$ and $KTaO_3$ by using the anharmonic dynamical matrices obtained at each temperature with results where the dynamical matrix was fixed to the one obtained at 150 K. This comparison shows that the temperature dependence of the dynamical matrices has a non-negligible contribution to the temperature behaviour of the mobility.

Lastly, we show in Fig. S11 that the inclusion of spin-orbit coupling (SOC) in the calculation of the electron mobility in $SrTiO_3$ brings little to no change with respect to spin-unpolarized calculations. This is due to the fact that the renormalized effective masses due to SOC are almost unchanged in $SrTiO_3$, as shown in Table SI, and the conduction-band splitting of 28 meV is too small to produce an increase in mobility. The masses in Table SI have been computed by parabolic fits on a range of points around the Γ-point that grants the minimum error on the fit parameters, as shown in Fig. S10. The results are in agreement with previous calculations [4,9]. As for $SrTiO_3$, the effective masses of $KTaO_3$ are rather unchanged by the inclusion of SOC (Table SI), however, the mobility is strongly enhanced due to SOC (Fig. 5 in the main text). This is mainly attributed to a large band splitting of 314 meV near the conduction-band bottom at the Γ-point.

In order to take into account potential non-parabolic behaviors around the Γ point, we adopt the Kane model [10] at the quasi-linear dispersion level [11]:

$$\frac{\hbar^2 k^2}{2m} = E(1+\alpha E), \tag{S8}$$

where m is the effective electron mass and α quantifies the deviation from the ideal parabolic behavior. We thus adopt a least square approach around the parabolic minimum, and keep α and m as fitting parameters. The

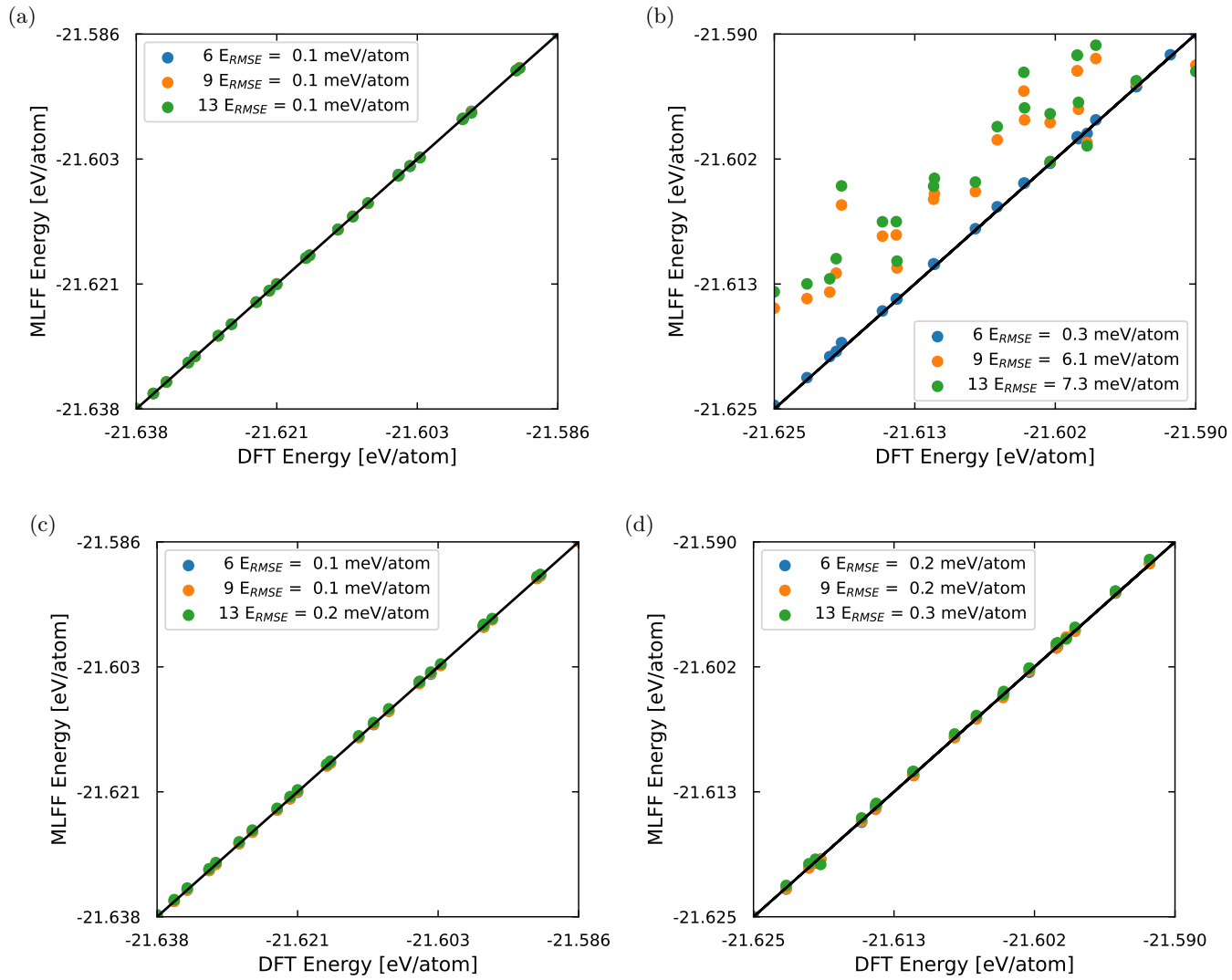

FIG. S6: Energy RMSE in $KTaO_3$ for 25 test structures of 320 atoms using different values for the cut-off radii of the descriptors. The MLFF trained on structures sampled on the fly during MD in the NVT ensemble is validated on different test sets of random structures sampled from (a) NVT and (b) NPT MD. The MLFF trained on additional 677 structures sampled from the NPT ensemble is validated on the same (c) NVT and (d) NPT random structures, showing a consistent behaviour.

only non-parabolicity is found for the heavy electron of $SrTiO_3$ on the Γ-X path in the case of SOC, as shown in Figure S12. The parabolic fit predicts an effective mass of 6.37 m_e (no SOC) and 1.10 m_e (SOC), while the Kane model predicts, respectively, 6.37 m_e and 0.89 m_e. The effective mass reduction due to SOC is thus accompanied by non-parabolicity. Surprisingly, in $KTaO_3$ no deviations from parabolicity are observed, and the Kane model coincides with a simple parabolic fit, despite the stronger SOC contribution on the band gap in $KTaO_3$ with respect to $SrTiO_3$.

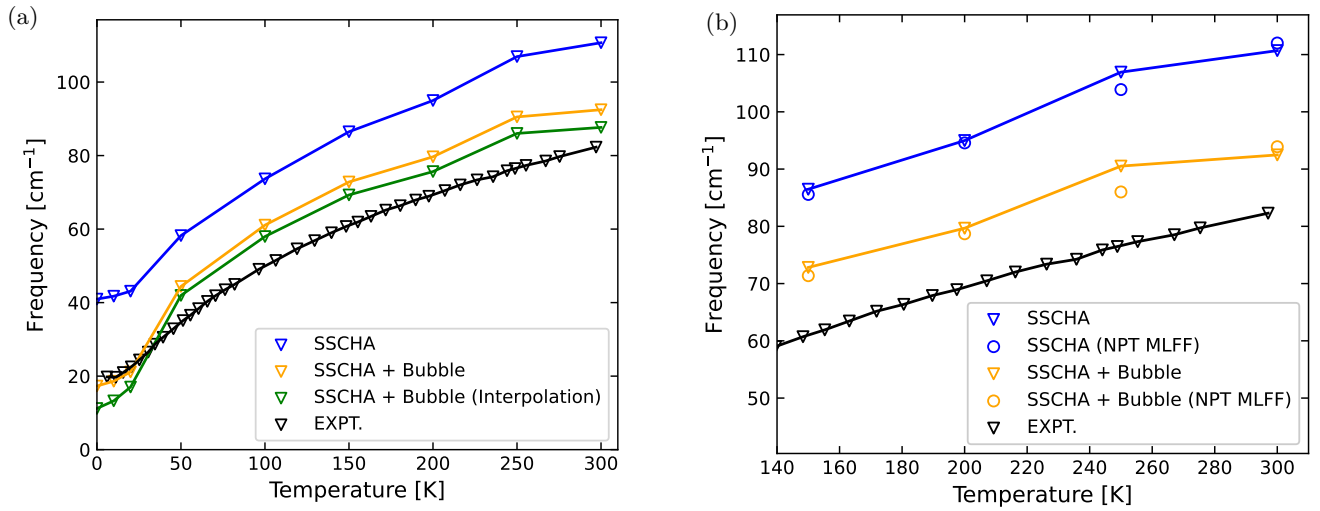

FIG. S7: Temperature dependence of the FE mode frequency at the Γ-point in $KTaO_3$, together with experimental data [8]. (a) SSCHA frequencies at different levels of approximation, as obtained by employing the NVT MLFF. (b) Comparison between the NVT and NPT MLFF results in the temperature range $150 - 300$ K.

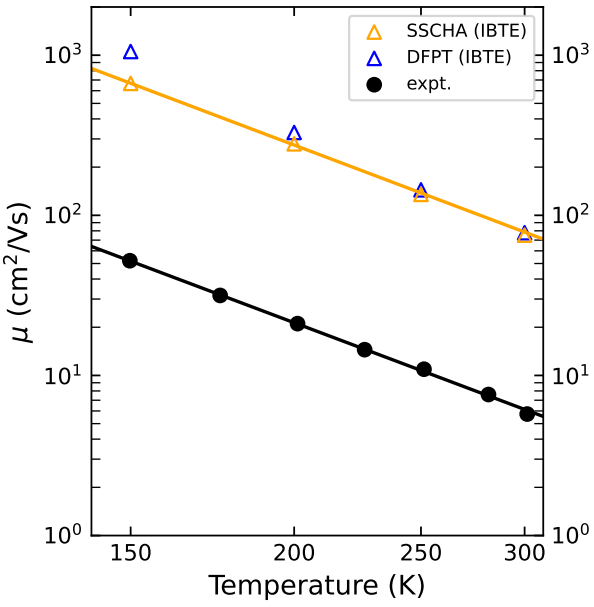

FIG. S8: Mobility in $SrTiO_3$ as computed from harmonic dynamical matrices with imaginary frequencies (blue markers) and from the SSCHA matrices (orange markers). The experimental data are in black.

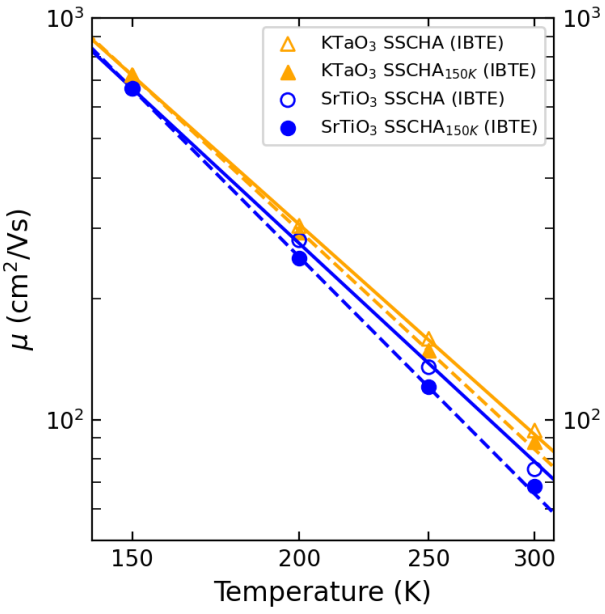

FIG. S9: Comparison of the mobilities obtained employing the correct SSCHA matrices at each temperature in $SrTiO_3$ (blue empty circles) and $KTaO_3$ (orange empty triangles) and the respective results using the SSCHA matrices calculated at 150 K (blue and orange filled markers).

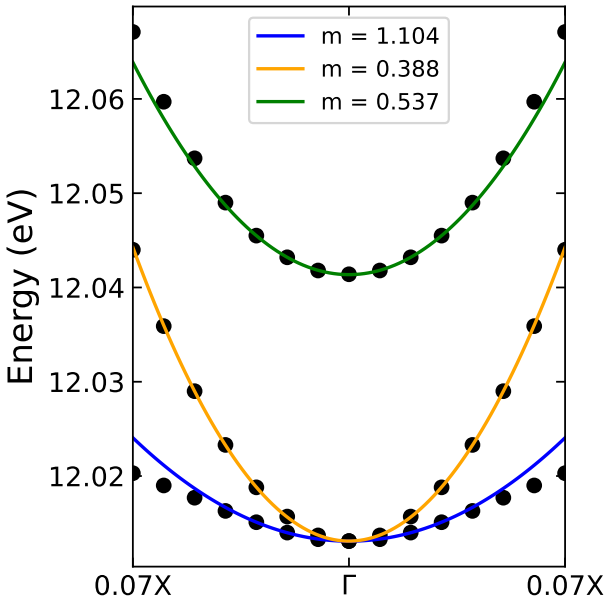

FIG. S10: Parabolic fit of the three bottom conduction bands in $SrTiO_3$, calculated with SOC. Each band is doubly degenerate. The electron effective masses are in units of the free electron mass.

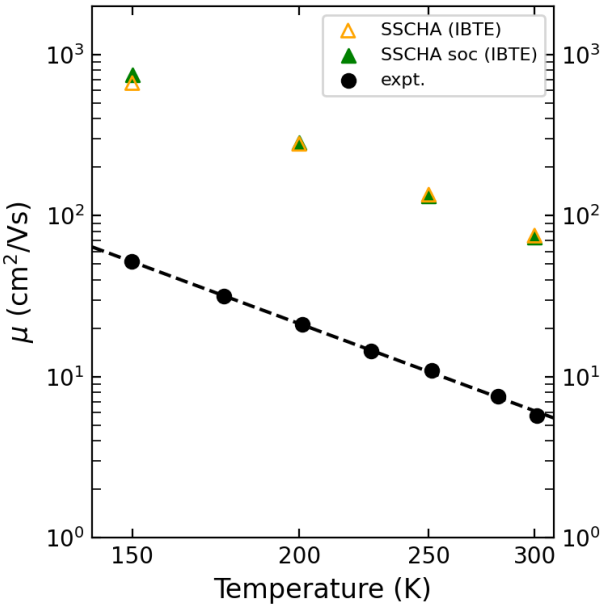

FIG. S11: Mobility in $SrTiO_3$ as computed from the SSCHA matrices including (green filled triangles) and neglecting (orange empty triangles) spin-orbit coupling. In black markers, the experimental data.

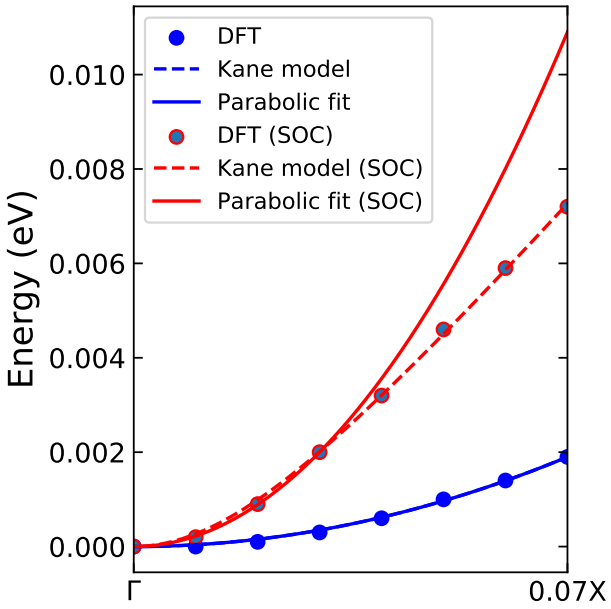

FIG. S12: Heavy electron band in SrTiO3 with SOC (red edged markers) and without (blue makers), in DFT. The parabolic fit and the least square minimization based on the Kane model are shown respectively in solid and dashed lines.

[1] J. Ziman, Electrons and phonons, Oxford University Press (1960).

[2] F. Giustino, Electron-phonon interactions from first principles, Rev. Mod. Phys. **89**, 015003 (2017).

[3] S. Baroni, S. de Gironcoli, A. Dal Corso, and P. Giannozzi, Phonons and related crystal properties from density-functional perturbation theory, Rev. Mod. Phys. **73**, 515 (2001).

[4] J.-J. Zhou, O. Hellman, and M. Bernardi, Electron-phonon scattering in the presence of soft modes and electron mobility in $srtio_3$ perovskite from first principles, Phys. Rev. Lett. **121**, 226603 (2018).

[5] X. Gonze and C. Lee, Dynamical matrices, born effective charges, dielectric permittivity tensors, and interatomic force constants from density-functional perturbation theory, Phys. Rev. B **55**, 10355 (1997).

[6] C. Verdi, L. Ranalli, C. Franchini, and G. Kresse, Quantum paraelectricity and structural phase transitions in strontium titanate beyond density functional theory, Phys. Rev. Mater. **7**, L030801 (2023).

[7] L. Monacelli, R. Bianco, M. Cherubini, M. Calandra, I. Errea, and F. Mauri, The stochastic self-consistent harmonic approximation: calculating vibrational properties of materials with full quantum and anharmonic effects, J. Condens. Matter Phys **33**, 363001 (2021).

[8] H. Vogt, Refined treatment of the model of linearly coupled anharmonic oscillators and its application to the temperature dependence of the zone-center soft-mode frequencies of $ktao_3$ and $srtio_3$, Phys. Rev. B **51**, 8046 (1995).

[9] M. Marques, L. K. Teles, V. Anjos, L. M. R. Scolfaro, J. R. Leite, V. N. Freire, G. A. Farias, and J. da Silva, E. F., Full-relativistic calculations of the SrTiO3 carrier effective masses and complex dielectric function, Appl. Phys. Lett. **82**, 3074 (2003).

[10] E. O. Kane, Band structure of indium antimonide, J. Phys. Chem. Sol. **1**, 249 (1957).

[11] L. D. Whalley, J. M. Frost, B. J. Morgan, and A. Walsh, Impact of nonparabolic electronic band structure on the optical and transport properties of photovoltaic materials, Phys. Rev. B **99**, 085207 (2019).